Tuning the ferroelectric-to-paraelectric transition temperature and dipole orientation of group-IV monochalcogenide monolayers

Salvador Barraza-Lopez, Thaneshwor P. Kaloni, Shiva P. Poudel, and Pradeep Kumar

Phys. Rev. B **97**, 024110 — Published 22 January 2018

DOI: 10.1103/PhysRevB.97.024110

Tuning the ferro- to para-electric transition temperature and dipole orientation of group-IV monochalcogenide monolayers

Salvador Barraza-Lopez,[1,2,*] Thaneshwor P. Kaloni,[1] Shiva P. Poudel,[1] and Pradeep Kumar[1]

[1] *Department of Physics, University of Arkansas, Fayetteville, AR 72701, USA*
[2] *Institute for Nanoscale Science and Engineering, University of Arkansas, Fayetteville, AR 72701, USA*

Coordination-related, two-dimensional (2D) structural phase transitions are a fascinating and novel facet of two-dimensional materials with structural degeneracies. Nevertheless, a unified theoretical account of these transitions remains absent, and the following points are established through *ab-initio* molecular dynamics and 2D discrete clock models here: Group-IV monochalcogenide (GeSe, SnSe, SnTe, ...) monolayers have four degenerate structural ground states, and a phase transition from a three-fold coordinated onto a five-fold coordinated structure takes place at finite temperature. On unstrained samples, this phase transition requires lattice parameters to evolve freely. A fundamental energy scale J permits understanding this transition, and numerical results indicate a transition temperature T_c of about $1.41J$. Numerical data provides a relation among the experimental (rhombic) parameter $\langle\Delta\alpha\rangle$ [*Science* **353**, 274 (2016)] and T of the form $\langle\Delta\alpha\rangle = \Delta\alpha(T=0)\,(1-T/T_c)^{\beta}$, with a critical exponent $\beta \simeq 1/3$ that coincides with experiment. It is also shown that $\langle\Delta\alpha\rangle$ is temperature-independent in *Phys. Rev. Lett.* **117**, 097601 (2016), and thus incompatible with experiment. T_c and the orientation of the in-plane intrinsic electric dipole can be controlled by moderate uniaxial tensile strain, and a modified discrete clock model describes the transition on strained samples qualitatively. An analysis of out-of-plane fluctuations, and a discussion of van der Waals corrections are given too. These results provide an experimentally-compatible framework to understand structural phase transitions in 2D materials and their effects on material properties.

I. INTRODUCTION

Besides well-understood out-of-plane corrugations,[1–4] there are exquisite and intriguing physical effects on 2D materials at finite temperature. For instance, some atomistic membranes can change their (average) atomistic coordination, without melting in the process.

Studies of structural phase transitions in two dimensions have a long and celebrated history[5–7] and find applications in ferromagnetism, biological and other types of membranes that may be dynamically or statically corrugated and can also conformally adapted onto a substrate, polymer networks, and other soft materials.[8] Two-dimensional (2D) materials are (atom-thick) membranes too, but not much has been said concerning structural phase transitions that are not driven by standard mechanisms such as crystal nonuniformities, defects, grain boundaries, impurities, electron irradiation,[9] but solely by structural degeneracies in these materials yet. This may be so because the most studied 2D materials, graphene[10,11] and transition-metal dichalcogenide monolayers on the 2H structure (2H-TMDMs)[12] have a single (and hence non-degenerate) highly-symmetric *structural* ground state.

But graphene and 2H-TMDMs may rather be an exception in terms of structural degeneracies in 2D materials. Indeed, despite of its structural similarity to graphene, hexagonal boron nitride monolayers[13] display a two-fold degeneracy by the exchange of boron and nitrogen atoms in their unit cells, silicene[14–16] has a two-fold degeneracy that is revealed by the exchange of upper and lower atoms in its buckled structure,[17,18] TMDMs on the 1T phase are degenerate with upon reflection with respect to the 2D plane, and TMDMs in the 1T' phase (having in-plane lattice vectors that form an angle smaller than sixty degrees) are three-fold degenerate.[19] Unlike square[5,7] or honeycomb lattices,[1] and as seen in Fig. 1(a), rectangular unit cells are degenerate too, by the exchange of long and short lattice constants, and display an anharmonic elastic energy profile that pushes the unit cell away from an unstable square configuration onto one out of two rectangular shapes with either $a_1 > a_2$ or $a_1 < a_2$. Therefore, 2D materials with rectangular unit cells such as black phosphorus (BP) and some group-IV monochalcogenide monolayers (GeSe, SnSe, SnTe, ...) are structurally degenerate as well. The initial two-fold degeneracy of the rectangular unit cell is aggravated by the disposition of basis atoms, and a reflection with respect to the axis perpendicular to the longest lattice vector yields an additional two-fold degeneracy, resulting in the four degenerate structural ground states[20–22] shown in Fig. 1(b).

Previous paragraph implies that reduced structural symmetries are, in fact, a rather pervasive feature of 2D materials[18,20–23] beyond graphene. We demonstrate in this manuscript that these structural degeneracies necessarily alter the way to think of thermal effects on atom-thick membranes: these structural degeneracies are the prime ingredient for observing 2D structural phase transitions that are quite intriguing and not a mainstream topic within the 2D materials community yet. Among other phenomena, structural degeneracies lead to non-harmonic phonon modes,[24] softened elastic constants, and to structural transitions that tune properties by tem-

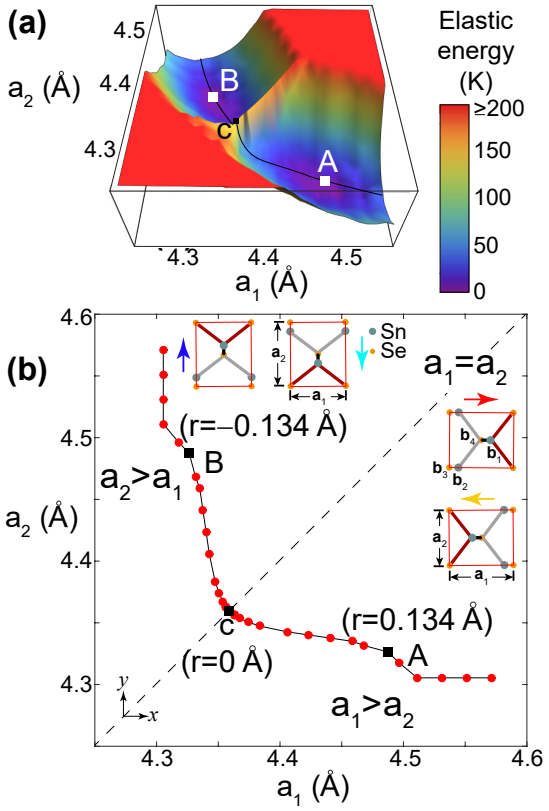

FIG. 1. (a) Zero-temperature energy landscape $E(a_1, a_2)$ of the unit cell of a SnSe monolayer. (b) Minimal energy pathway $E(r(a_1, a_2))$ on landscape, joining degenerate structural ground states $A_{\rightarrow}$ and $A_{\leftarrow}$ (both located at $r = 0.134$ Å) to $B_{\uparrow}$ and $B_{\downarrow}$ (at $r = -0.134$ Å), through the saddle point c.

perature (T).

BP monolayers cannot undergo 2D structural transitions and melt directly,[20] making structural degeneracies a necessary but insufficient condition for realizing such structural phase transitions.

Although many group-IV monochalcogenide monolayers do undergo experimentally-verified coordination-related structural transitions,[20,23,25] the present understanding of these materials at finite temperature remains work in progress. A sign of the early stage of these investigations is the huge spread in theoretical estimations of the transition (Curie, critical) temperature T_c[23,26] for identical group-IV monochalcogenide monolayers, and the relation among a fundamental scale J to be soon defined, and T_c –either $T_c \simeq 1.17J$[23] or $T_c \simeq 6J$[26]– that ought to be addressed. Beyond these estimates, the thermal behavior of these two-dimensional materials provides connections among hard- and soft-condensed matter, making these results of interest to a broad audience.

To achieve a unified description of 2D structural phase transitions in group-IV monochalcogenide monolayers, the three overarching conditions for the existence of 2D structural phase transitions are enunciated in Section II. Then, the differences among the two existent theoretical models describing the ferro-to-paraelectric phase transition in group-IV monochalcogenide monolayers are indicated in Section III; one of them (called Model 1 henceforth) is based on the NPT ensemble[20,23] (constant number of atoms, *pressure*, and temperature), while the other (Model 2) is based on a NVT ensemble[26] (constant number of atoms, *volume*, and temperature). It is shown that the volume constraint on the latter model yields temperature-independent lattice parameters a_1 and a_2 that are inconsistent with experiment, thus leading to an overestimation of T_c, as can be gathered from an analysis of the relevant energy scale of these structures (J) in Section IV. In Sections V and VI, the tunability of T_c by uniaxial tensile strain is shown, which also permits orienting the direction of the in-plane intrinsic electric dipole after a threshold amount of strain is applied. Section VII showcases a two-parameter model that describes all observed details of these transitions qualitatively. The results provided here are aimed to unify and to guide what are at the moment conflicting theoretical accounts of these structural transitions.[23,26] Conclusions are provided afterwards.

Considering readability for a wide audience, a deliberate effort is made to highlight physical behavior over numerics. Basically, we report DFT calculations employing the *SIESTA* code[27] with van der Waals corrections[28] on a SnSe monolayer unit cell in Figs. 1 to 2 that permit defining an elastic energy landscape with degenerate minima, and an intrinsic energy scale J. Afterwards, the evolution of order parameters is studied through *ab initio* molecular dynamics on 8×8 and 16×16 supercells on the NPT ensemble. The use of different supercell sizes permits assessing the dependence of T_c on system size. The manuscript ends by describing the effects of uniaxial strain on T_c qualitatively, employing 8×8 supercells for that purpose. All *ab initio* calculations are performed on structures that have a separation of 20 Å among periodic vertical images. Results of model calculations that were computed with Monte Carlo methods are presented along the way. Detailed and additional descriptions of computational methods –that permit reproducing these results– are given in Appendix A.

Although the material chosen here is SnSe, the results here are meant to describe the general behavior of group-IV monochalcogenide monolayers with rectangular unit cells at zero temperature.

II. CONDITIONS FOR THE OCCURRENCE OF 2D STRUCTURAL PHASE TRANSITIONS

To create 2D structural phase transitions, the degeneracies indicated in previous Section must be complemented by two additional conditions that are illustrated on a SnSe monolayer next:

1. In the elastic energy landscape[29] $E(a_1, a_2)$ shown in Fig. 1(a), an energy pathway must exist that is

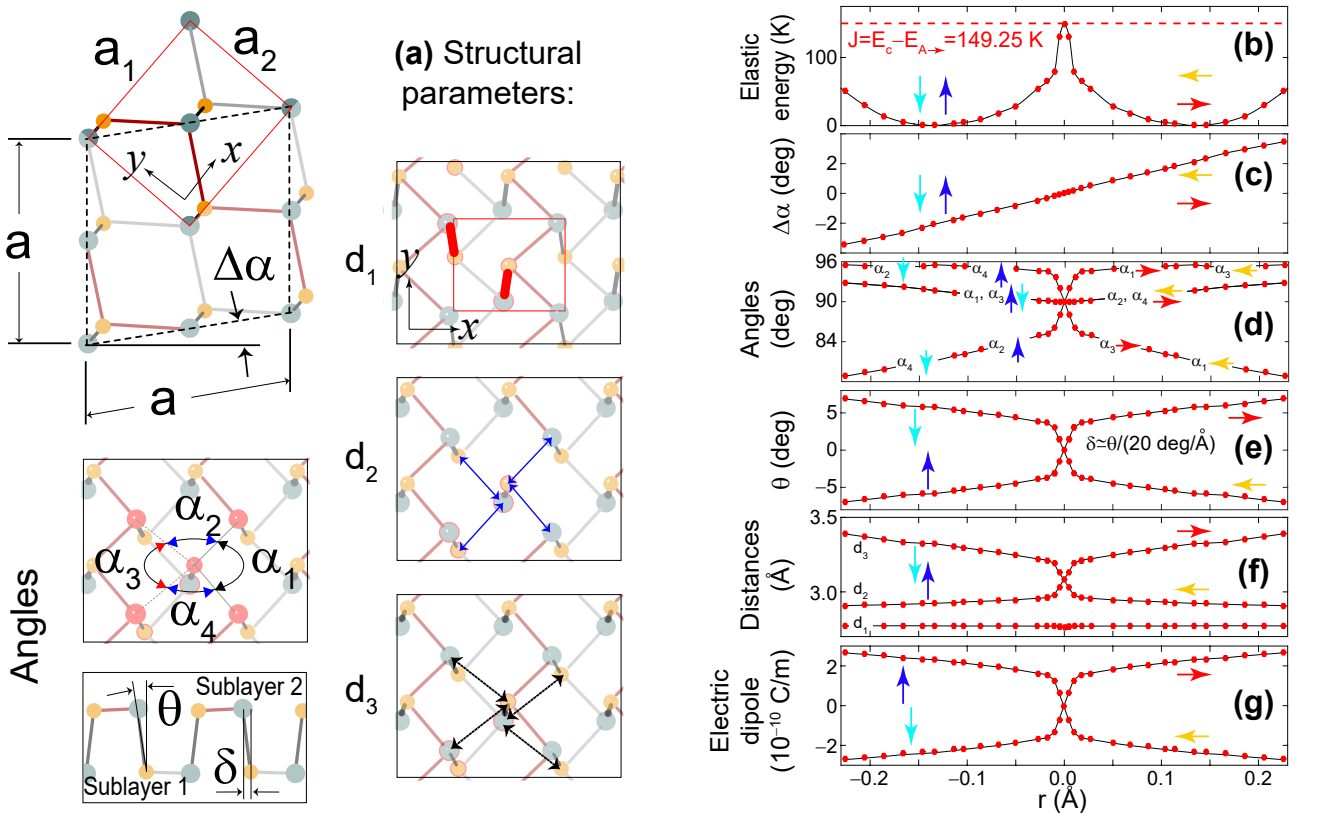

FIG. 2. (a) Structural order parameters that signal 2D phase transitions. Zero-temperature evolution of (b) structural (elastic) energy, order parameters (c) $\Delta\alpha$, (d) angles α_1, α_2, α_3, (e) θ, δ, (f) interatomic distances d_1, d_2, d_3 and (g) electric dipole as a function of r, for the four possible unit cells. All order parameters on subplots (b-g) depend on r and therefore, on a_1 and a_2 predominantly evolving along the low-energy path drawn in Fig. 1.

highlighted as $r(a_1, a_2)$ in Fig. 1(b) and joins pairs of degenerate ground states. The joining paths are labeled $A_{\rightarrow} \leftrightarrow B_{\uparrow}$, $A_{\rightarrow} \leftrightarrow B_{\downarrow}$, $A_{\leftarrow} \leftrightarrow B_{\uparrow}$, or $A_{\leftarrow} \leftrightarrow B_{\downarrow}$ and proceed against an energy barrier $J \equiv (E_c - E_{A_{\rightarrow}}) < k_B T_m$ at point c, where T_m is the material's melting point, k_B is Boltzmann's constant, and E_c is the smallest structural energy along the $a_1 = a_2$ line ($E_c = min\{E(a_1, a_1)\}$) on a structure lacking electric polarization (hence the omission of arrows on E_c). Horizontal (vertical) arrows indicate a net dipole moment along the $x-$ ($y-$)direction.[20] Unit cells switch among any of the *four* degenerate structures once the barrier J is overcome.[5,20]

2. Thermodynamic equilibrium requires degenerate ground states to be evenly sampled, and this implies that macroscopic domains representing the four degenerate ground states will be visible on a sample. Therefore, the second condition is that sufficiently large domains exist below T_c. This condition is verified by experiment.[25]

When structural degeneracies exist and conditions (1-2) are satisfied, 2D structural phase transitions alter the properties of 2D materials in ways that are only beginning to be studied.[20,22,23,26]

As displayed in Fig. 2(a), $\Delta\alpha$ is a geometrical variable motivated by experiment[25] that signals a departure from a square unit cell ($\Delta\alpha = 0$ and $a_1 = a_2$) onto a rhombus ($\Delta\alpha \neq 0$ and $a_1 \neq a_2$). In Fig. 2(a), the long and short diagonals of the rhombus are orthogonal, and have magnitudes $2a_1$ and $2a_2$, respectively.

Experimentally, the 2D structural transition was linked to a sudden collapse of $\Delta\alpha$ to zero[25] which, in turn, requires a sudden change of lattice parameters at the Curie temperature T_c onto $a_1/a_2 = 1$,[20,23] (see Fig. 2(a) and Appendix B):

$$\frac{a_1(r)}{a_2(r)} = \frac{1 + \sin\Delta\alpha(r)}{\cos\Delta\alpha(r)} (\simeq 1 + \Delta\alpha(r) \text{ for } \Delta\alpha(r) \simeq 0). \quad (1)$$

According to Eqn. (1), $\Delta\alpha = 0$[25] implies $a_1 = a_2$[20,23] and $r = 0$ in Fig. 1(b). The reader must note that no other theory exists at this moment that reproduces this experimental fact.

Besides $\Delta\alpha$, the four local basis atoms at any given unit cell ($\mathbf{b}_i$, $i = 1, 2, 3, 4$) confer this 2D material with additional structural order parameters: distances $d_1 = |\mathbf{b}_3 - \mathbf{b}_2|$, $d_2 = |\mathbf{b}_4 - \mathbf{b}_2|$, and $d_3 = |\mathbf{b}_4 - \mathbf{b}_2 + \mathbf{a}_1|$; angles $\alpha_1 = \angle(\mathbf{b}_2 + \mathbf{a}_1, \mathbf{b}_4, \mathbf{b}_2 + \mathbf{a}_1 + \mathbf{a}_2)$, $\alpha_2 = \angle(\mathbf{b}_2 +$

$\mathbf{a}_1+\mathbf{a}_2, \mathbf{b}_4, \mathbf{b}_2+\mathbf{a}_2$), $\alpha_3 = \angle(\mathbf{b}_2+\mathbf{a}_2, \mathbf{b}_4, \mathbf{b}_2)$ and $\alpha_4 = \angle(\mathbf{b}_2, \mathbf{b}_4, \mathbf{b}_2+\mathbf{a}_1)$; the angle $\theta = \text{acos}\left[(\mathbf{b}_4-\mathbf{b}_1)\cdot\hat{z}/|\mathbf{b}_4-\mathbf{b}_1|\right]$,[26]; and $\delta = (\mathbf{b}_1-\mathbf{b}_4)\cdot\frac{\mathbf{a}_1}{|\mathbf{a}_1|}$, the projection of the $\mathbf{b}_1-\mathbf{b}_4$ vector onto the local $x-$axis. $\hat{z}$ is the local normal to the corrugated 2D material.[30–33]

Considering structure $A_{\rightarrow}$ for reference, the interdependence of δ and θ on $a_1(r)$, $d_1(r)$, and $\alpha_1(r)$ in Fig. 2 is as follows:

$$\delta = \frac{a_1}{2} - d_2\cos\left(\frac{\alpha_1}{2}\right), \text{ and } \theta = \arcsin\left(\frac{\delta}{d_1}\right). \qquad (2)$$

In order for the dipole moment to point along the positive $x-$direction, the chalcogen atom (1 and 3) has an $x-$coordinate smaller than the $x-$coordinate of the group-IV atom ($b_{1x} < b_{3x}$, and $b_{2x} < b_{4x}$).

$E(r)$ in Fig. 2(b) is a one-dimensional cut of the elastic energy landscape, Fig. 1(a), along the minumum energy line $r(a_1, a_2)$ displayed as Fig. 1(b), that emphasizes the four degenerate ground states ($A_{\rightarrow}$, $A_{\leftarrow}$, $B_{\uparrow}$ and $B_{\downarrow}$). This energy profile has a direct dependence on a_1 and a_2, as it requires both lattice parameters to vary. Negative values of r in Fig. 1(b) –occurring for values of a_1 and a_2 such that $a_2 > a_1$– correspond to structures with an electric dipole oriented along the vertical direction, while positive values of r –taking place when $a_2 < a_1$– describe structures with a horizontal electric dipole. $E(r)$ displays a cusp-like feature at $r = 0$ (point c in Fig. 1(b)), representing a square structure with a zero net electric dipole. The existence of two minima points A and B in Figs. 1(a) and 1(b)) implies that the elastic energy profile is anharmonic.[34]

When discussing the stability of 2D materials, Fasolino, Loss and Katsnelson argue that anharmonic contributions to the elastic energy, that are absent in the Mermin-Wagner theorem,[7] are crucial to understand long-range order in 2D materials. The anharmonic contribution in graphene is due to the coupling of in-plane (stretching) and out-of-plane (bending) vibrational modes.[1] As shown in Fig. 2(b), group-IV monochalcogenide monolayers have an anharmonic elastic profile even without considering out-of-plane bending, that may render Mermin-Wagner theorem unapplicable as well. (The extent of out-of-plane bending of SnSe monolayers at finite temperature will be discussed later.)

In Figs. 2(c) to 2(f), the dependence of order parameters on r are shown for the four possible structures that were labeled with colored arrows, while Fig. 2(g) displays the dependence of the in-plane electric dipole on r.

Numerical details aside, the points from Fig. 1 are as follows: (a) there are four degenerate ground states on group-IV monochalcogenide monolayers and (b) a single characteristic energy barrier J to describe this 2D transition;[20] (c) the in-plane structural transition is driven by a sudden collapse of a_1/a_2 to unity.[20,23]

III. NPT ENSEMBLE AND THE FERRO- TO PARA-ELECTRIC TRANSITION

A. Thermal evolution of out-of-plane corrugations, order parameters, and configuration energy

The zero-temperature evolution of order parameters as a function of r in Figs. 2(c) to 2(g) provides insight into the structural properties of this material family at finite temperature as long as r (and hence a_1 and a_2) varies with T: molecular dynamics (MD) calculations at finite temperature carried out within the NPT ensemble (constant number of particles, constant pressure, and constant temperature) allow the lattice parameters and hence r to adapt with T.[20] In fact, allowing a_1 and a_2 to vary is standard practice in studies of 2D materials at finite temperature.[1]

One employs condition 2 from Sec. 1 and builds 8×8 and 16×16 supercells with atoms on the ground state $A_{\rightarrow}$ configuration; *i.e.*, domain $A_{\rightarrow}$ is set as the initial structure at zero Kelvin. The *ab initio* MD trends for the 8×8 supercell (256 atoms and 20,000 fs time duration) can be obtained in three months, while the trends for the 16×16 supercell (1024 atoms and 20,000 fs) are completed in nine months. Further details of MD calculations can be found in Appendix A. From now on, parameters within angular brackets represent thermal averages.

Membrane corrugations are *global* distortions that can be characterized by the largest height difference Δz at each supercell time-frame. Given the material tickness of $z_0 = 2.801$ at $T = 0$, and the shortest side of the supercell L_{min} on the same time-frame, the (percent) vertical deviation shown in Fig. 3(a) given by $(\Delta z - z_0)\times 100/L_{min}$ is consistent with result reported on other 2D materials[1–4] for the two supercells in present calculations.

Besides the height of out-of-plane oscillations, it is possible to define *local* structural variables too. For example, using the precepts from Ref. 33, a local discrete geometry was introduced to describe the local shape of 2D crystals in Refs. 30–32. In a similar manner, all variables in Fig. 2(a) are defined at individual unit cells and are hence local.

Figure 3(b) displays the thermal evolution of $\langle r\rangle$ towards zero past T_c. The larger path in Fig. 3(b) when contrasted with the value of r at point A in the zero-temperature plot (Fig. 1(b)) has to do with the thermal expansion of the unit cell at finite temperature.

Using Eqn. (1), $\langle a_1\rangle$ and $\langle a_2\rangle$ obtained from MD runs for SnSe monolayers and bilayers are recast onto the $\langle\Delta\alpha\rangle$ *versus* temperature plot in Fig. 3(c), which constitutes one of main results of this manuscript. The evolution of $\langle\Delta\alpha\rangle$ on few-layer SnTe in Ref. 25 leads to a Curie's temperature T_c that is determined by (i) a sudden collapse of $\langle\Delta\alpha\rangle$ to zero, and (ii) T_c increases with the number of layers. Experimental features (i) and (ii) are generic to few-layer monochalcogenides, and captured in Fig. 3(c) for SnSe monolayers and bilayers. This structural transition takes place within 800 fs in our MD calculations, an

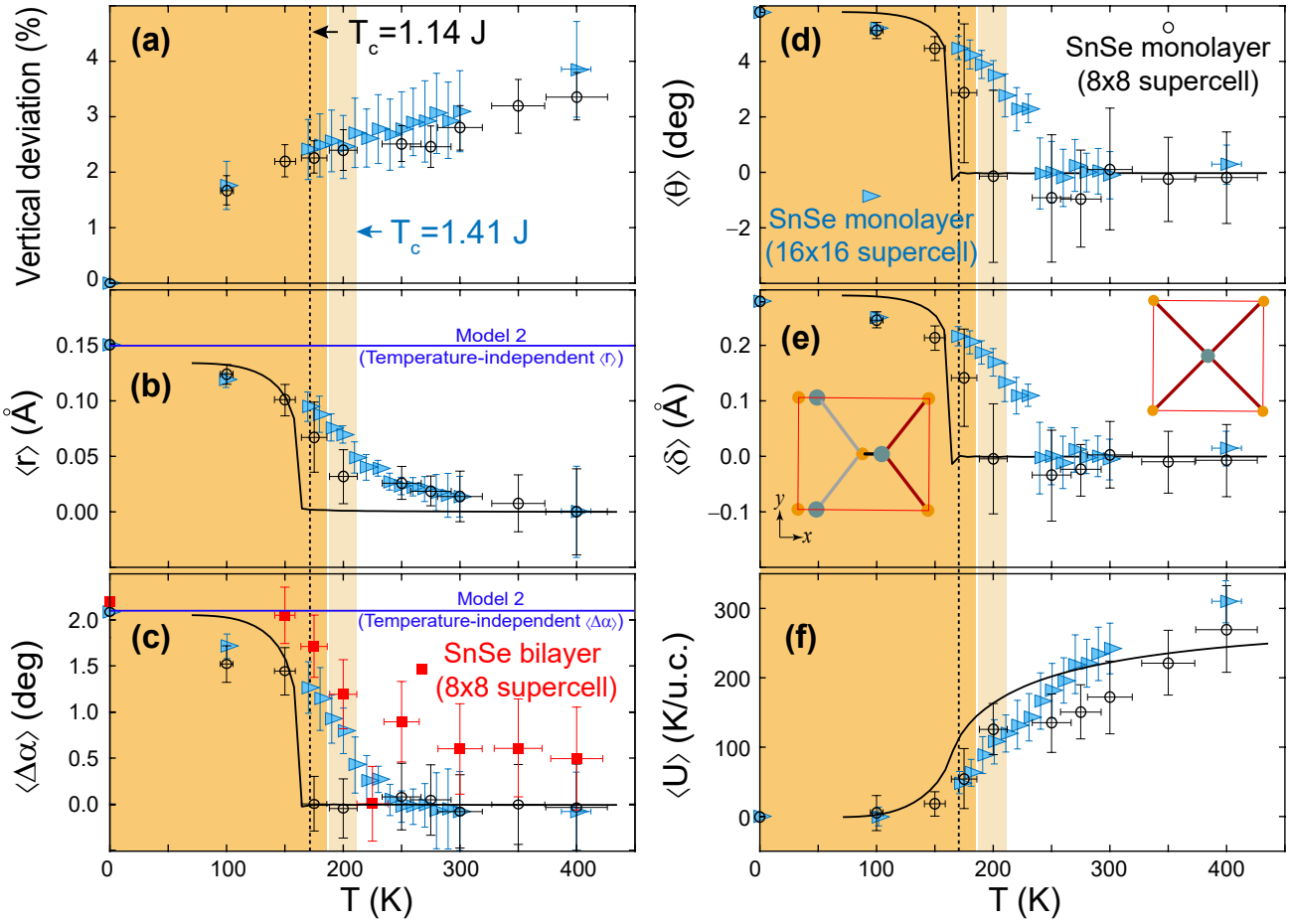

FIG. 3. Thermal evolution of (a) the out-of-plane fluctuations at T_c (which is smaller than 3% and is expressed in terms of the shortest in-plane side), (b) $\langle r\rangle$, (c) $\langle\Delta\alpha\rangle$, (d) $\langle\theta\rangle$, (e) $\langle\delta\rangle$ and (f) configuration energy $\langle U\rangle$ for SnSe monolayers on 8×8 (open circles) and 16×16 supercells (filled triangles), showing a dependency of T_c with system size. $\langle\rangle$ stands for thermal averages. $\langle\theta\rangle$, $\langle\delta\rangle$, $\langle r\rangle$, and $\langle\Delta\alpha\rangle$ all turn to zero near T_c. $\langle\Delta\alpha\rangle$ is also shown for a SnSe bilayer, which displays a larger T_c. Straight lines in (d) and (e) display the independence of $\langle r\rangle$ and $\langle\Delta\alpha\rangle$ on temperature in the NVT ensemble. Fits in continuum solid black originate from a discrete clock model.

ultra-fast time that is even consistent with experimental switching times on ultrathin chalcogen-based materials.[35]

Structural variables θ and δ in Fig. 2(a) and Eqn. (4) turn the in-plane electric dipole off at point c ($r = 0$) at T_c, which represents a square unit cell. In a similar fashion, $\langle\theta\rangle$ and $\langle\delta\rangle$ in Figs. 3(d) and 3(e) correlate with the vanishing of $\langle r\rangle$ in Fig. 3(d) when thermally driven on MD runs.

The structural contribution $\langle U\rangle$ to the total energy in the MD calculation is a result of the structural evolution, and it is displayed in Fig. 3(f), showing a sudden increase at T_c which implies, by virtue of Figs. 1(a) and 2(b), the expected transition onto a square structure.

Indeed, starting on a structure originally consistent with the $A_{\rightarrow}$ structural ground state, Fig. 3(f) demonstrates that temperature drives the structural energy $\langle U\rangle$ up, making all other three structures ($B_{\uparrow}$, $B_{\downarrow}$, and accordingly $A_{\leftarrow}$) accessible, and thus driving the 2D structural transition. $\langle U\rangle$ is listed per unit cell in order to write it in units of temperature, which is an intensive quantity. The (yellow) boxes in Fig. 3 highlight the magnitude of T_c obtained in MD calculations of SnSe monolayers without uniaxial strain, which increased with system size, as shown in the figure.

To emphasize, materials without structural degeneracies will not develop a sudden structural change as the one described by the local variables in Fig. 3(b-e): these structural changes occur once the material –originally set at one of the four degenerate structural ground states– has sufficient energy to explore all four degenerate structures, thus turning onto a structure with an increased structural symmetry, on average. In his celebrated book, Volovik argues for symmetry breaking at low temperatures, and the (average) enhancement of symmetry at a critical temperature T_c,[36] is consistent with such fundamental physical insight.

In our calculations with standard out-of-plane fluctuations, the local magnitudes of a_1 and a_2 are inter-

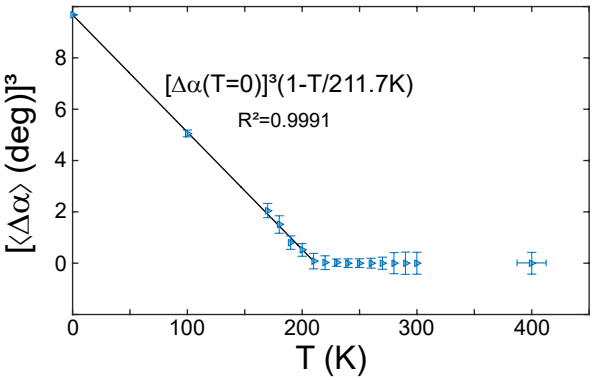

FIG. 4. Linear relation among $\langle\Delta\alpha\rangle^3$ and T. A fit to the data yields $T_c = 212 \pm 7$ K.

atomic distances among identical basis atoms located at the nearest neighboring unit cells. In Fig. 4, the relation between $\Delta\alpha$ and a_1/a_2, Eqn. (1), leads to a thermal behavior of $\langle\Delta\alpha\rangle$ of the following form:

$$\langle\Delta\alpha\rangle = \Delta\alpha(T=0)\left(\frac{T_c - T}{T_c}\right)^{\frac{1}{3}}, \tag{3}$$

with $T_c = 212 \pm 7$ K. The results here contained not only reproduce the experimental collapse of $\langle\Delta\alpha\rangle$ to zero. Remarkably, and as a statement to their accuracy and significance to experiment, they also reproduce the experimental critical exponent, $\beta = 1/3$.

B. Phenomenological model to understand the transition qualitatively

The trendlines are the result from Potts model, which takes J as its only (fitting) parameter, and whose methodology will be described now.

A phenomenological order-disorder model for two-dimensional phase transitions in two-dimensional crystals with four nearest-neighbors interactions and four degenerate ground states was developed some time ago.[5] Drawing an analogy between in-plane electric dipoles pointing along four discrete orientations and spins, T_c can be estimated from a discrete 2D clock model to be:[5,20]

$$T_c = 1.1(4)J/k_B. \tag{4}$$

(Potts writes $\frac{2J}{k_B T_c} = 1.76$ for the $r = 4$ structural ground states in the present problem.)

In our case, and as depicted in Fig. 3, $T_c = 175 \pm 11K$ on the 8×8 supercell, and $212 \pm 7K$ on the 16×16 supercell, amounting to $T_c = 1.17J/k_B$, and $T_c = 1.41J/k_B$ for a better converged estimation, respectively. This way, Potts model provides a phenomenological lower limit for the relation among T_c and J due to its simplified nature.

C. Constant $\langle\Delta\alpha\rangle$ with temperature on Fei *et al.* model

While the results in Fig. 3(e) do reproduce the experimental drop of $\langle\Delta\alpha\rangle$ to 0 at T_c, the thermal behavior of a structure with temperature-independent lattice parameters, Model 2,[26,37] is described by the NVT ensemble, where the area of the 2D material is kept fixed during the thermal evolution.

Independency of lattice parameters with temperature[26] yields $\partial(\langle\frac{a_1}{a_2}\rangle)/\partial T = 0$ and, using Eqn. (1):

$$\partial\langle\Delta\alpha\rangle/\partial T = 0, \tag{5}$$

which is inconsistent both with experimental observation[25] and this and previous[20,23] work. In Figs. 3(d-e), $\langle r\rangle$ and $\langle\Delta\alpha\rangle$ in Model 2 take constant, temperature-independent values that are emphasized by straight (blue) lines.

In addition to having a temperature-independent $\langle\Delta\alpha\rangle$ (and hence no critical exponent relating $\langle\Delta\alpha\rangle$ and T either), the relation among T_c and J is overestimated in Model 2. Working with SnSe as a representative example, the best estimate for T_c obtained from *ab initio* MD calculations in this work (Model 1) is 212 K, but $T_c = 326$ K in Model 2.[26] Such discrepancy may hamper further work on the area, as both estimations were made with the same underlying numerical approach (pseudopotential-based density functional theory), and deserves careful attention.

The discrepancy on T_c is resolved by first reaching an agreement on the intrinsic energy scale that triggers the structural transition. This appears necessary, as even reported values of a_1 and a_2 display a large scatter of 4.35–4.70 and 4.24–4.40, respectively[38–44] that affects estimates of J directly and of T_c subsequently.

IV. INTRINSIC ENERGY SCALE J FOR PHASE TRANSITIONS ON 2D MATERIALS WITH STRUCTURAL DEGENERACIES

A. Generic lattice and basis vectors needed to compute J

The intrinsic energy scale on materials with structural degeneracies is given by the energy difference among the (degenerate, rectangular) ground state unit cell, and the unit cell with high symmetry at zero temperature.

As indicated by condition 1 in Section II, the energy difference among the square unit cell (E_c) and the energy for a structure in the ground state ($E_{A_\rightarrow}$) yields J, which will be estimated in a detailed manner next.

Lattice vectors for the (square) unit cell at point c in Fig. 1(b) are given by:

$$\begin{aligned}\mathbf{a}_1 &= (a_c, 0, 0),\ \mathbf{a}_2 = (0, a_c, 0),\\ \mathbf{a}_3 &= (0, 0, 20\ \text{Å}),\end{aligned} \tag{6}$$

while the basis vectors (that yield a zero net electric

TABLE I. Optimal magnitudes for lattice and basis vectors listed in Eqns. (6) through Eqn. (9), and energy barrier J of SnSe monolayers, as obtained with three commonly used computational tools; van der Waals corrections are included in these estimates. Subindex c refers to the square structure at point c, while subindex A is to label the structural ground state A; c.f., Figs. 1(a)-(b). z_{2c} and z_{2A} are 0 Å throughout.

VASP, vdW.[45–48]
$J=(E_c-E_{A_\rightarrow})/k_B=154.84$ K; $\Delta\alpha(T=0)=2.298^o$
$a_c=4.3418$, $z_{1c}=2.8129$, $z_{3c}=2.7347$, $z_{4c}=0.0781$
$a_{1A}=4.4678$, $a_{2A}=4.2957$
$\delta=0.2879$, $z_{1A}=2.8641$, $z_{3A}=2.7309$, $z_{4A}=0.1331$
$a_{1A}/a_{2A}=1.0401$, $a_{1A}/a_C=1.0290$
Quantum Espresso, vdW.[49–54]
$J=(E_c-E_{A_\rightarrow})/k_B=146.04$ K; $\Delta\alpha(T=0)=2.097^o$
$a_c=4.3137$, $z_{1c}=2.8422$, $z_{3c}=2.7202$, $z_{4c}=0.1220$
$a_{1A}=4.4251$, $a_{2A}=4.2690$
$\delta=0.2684$, $z_{1A}=2.8593$, $z_{3A}=2.7180$, $z_{4A}=0.1417$
$a_{1A}/a_{2A}=1.0366$, $a_{1A}/a_C=1.0258$
SIESTA, vdW.[27,28,55,56]
$J=(E_c-E_{A_\rightarrow})/k_B=149.26$ K; $\Delta\alpha(T=0)=2.131^o$
$a_c=4.3590$, $z_{1c}=2.7661$, $z_{3c}=2.7616$, $z_{4c}=0.0042$
$a_{1A}=4.4873$, $a_{2A}=4.3264$
$\delta=0.2785$, $z_{1A}=2.8035$, $z_{3A}=2.7578$, $z_{4A}=0.0457$
$a_{1A}/a_{2A}=1.0372$, $a_{1A}/a_C=1.0294$

dipole given that $\theta=0$) are:

$$\begin{aligned}\mathbf{b}_1=&(a_c/2,a_c/2,z_{1c})\ \text{(Sn)},\\ \mathbf{b}_2=&\ (0,0,0)\ \text{(Sn)},\\ \mathbf{b}_3=&\ (0,0,z_{3c})\ \text{(Se)},\\ \mathbf{b}_4=&\ (a_c/2,a_c/2,z_{4c})\ \text{(Se)},\end{aligned}\tag{7}$$

where the atomic species are indicated. a_c, z_{2c}, z_{3c}, and z_{4c}, as obtained with van der Waals corrections appear in Table I (numerical details are given in Section A).

The magnitude of a_c in Table I renders the minimal energy of a unit cell under the constraint $a_1=a_2$ on a structure that lacks an in-plane electric dipole (Eqn. 7), as necessary for all four dipole orientations to occur with equal probability as soon as $a_1\neq a_2$. Point c is a saddle point on the elastic energy landscape $E(a_1,a_2)$ in Fig. 1(a): a minimum along the $a_1=a_2$ line, and a maximum along the (orthogonal) $r-$line in Fig. 2(b).

The ground state structures $A_\rightarrow$ and $A_\leftarrow$ have the following lattice vectors:

$$\begin{aligned}\mathbf{a}_1=&(a_{1A},0,0),\ \mathbf{a}_2=(0,a_{2A},0),\\ \mathbf{a}_3=&\ (0,0,20\ \text{Å}).\end{aligned}\tag{8}$$

The values of a_{1A} and a_{2A} in Tables I and II are guaranteed to yield the minimum energy by an explicit meshing procedure for a_1 and a_2 around point A that gives higher structural energies for values of a_1 and a_2 in the closest vicinity of the listed a_{1A} and a_{2A}, that can thus be considered reliable (DFT-vdW) mean field values. The basis

TABLE II. Lattice and basis vectors for structures employed to obtain SnSe energy barrier using identical methods and computational tool as in Ref.[26]. b_{2zc} and b_{2zc} are 0 Å throughout. Note that lack of van der Waals corrections yields a ratio a_{1A}/a_{2A} smaller than the one listed in Table I.

VASP, PBE.[45,46,57]
$J=(E_c-E_{A_\rightarrow})/k_B=50.30$ K; $\Delta\alpha(T=0)=1.175^o$
$a_c=4.3179$, $z_{1c}=2.7256$, $z_{3c}=2.7180$, $z_{4c}=0.0077$
$a_{1A}=4.3819$, $a_{2A}=4.2940$
$\delta=0.2106$, $z_{1A}=2.7505$, $z_{3A}=2.7167$, $z_{4A}=0.0338$
$a_{1A}/a_{2A}=1.0205$, $a_{1A}/a_C=1.0148$

vectors of a ground state structure are:

$$\begin{aligned}\mathbf{b}_1=&(a_{1A}/2\pm\delta,a_{2A}/2,z_{1A})\ \text{(Sn)},\\ \mathbf{b}_2=&\ (\pm\delta,0,0)\ \text{(Sn)},\\ \mathbf{b}_3=&\ (0,0,z_{3A})\ \text{(Se)},\\ \mathbf{b}_4=&\ (a_{1A}/2,a_{2A}/2,z_{4A})\ \text{(Se)},\end{aligned}\tag{9}$$

where a positive (negative) sign renders structure $A_\rightarrow$ ($A_\leftarrow$) that has an in-plane dipole moment that is oriented towards the positive (negative) $x-$axis, as confirmed by Bader charge analysis and Berry-phase calculations. Exchange of $x-$ and $y-$ components on both lattice and basis vectors renders the two additional degenerate structures $B_\uparrow$ and $B_\downarrow$.

B. Relevance of van der Waals corrections on 2D materials hosting lone pairs

According to Ref. 20, the ratio of lattice parameters a_1/a_2 for group IV monochalcogenide monolayers tends to unity as a function of the mean atomic number. Our calculations indicate that the value of the mean atomic number for which $a_1/a_2=1$ is highly dependent on the exchange-correlation functional employed, with structures computed with LDA turning into squares for smaller mean atomic number than structures obtained with PBE functionals. In turn, van der Waals corrections yield rectangular structures in cases where PBE predicts square unit cells.

Turning to experiment, the discovery of ferroelectricity on SnTe monolayers implies that this material hosts a rectangular unit cell,[25] while mean-field structural calculations with DFT and the PBE approximation indicate the unit cell to be square.[20,26]

Using SnSe as a representative case example, it will be shown that van der Waals corrections help increase the anisotropy among a_1 and a_2 on group-IV monochalcogenides, *even at the monolayer limit*,[23] and may lead to structural estimates that are closer to experiment.

Indeed, the energy barrier obtained for a SnSe monolayer in Table II follows the exact methodology and the numerical code listed in Model 2. (They indicate that no van der Waals corrections were included in monolayer

calculations.) The value $J = 50.3\ K$ for the SnSe monolayer is similar to the previously reported value,[26] and smaller to the magnitude of 146.0–154.8 obtained with van der Waals corrections in Table I.

Van der Waals corrections play an important role on non-covalent interactions, such as those originating from lone-pairs.[58] The four-fold degeneracy of monochalcogenide monolayers is the result of a three-fold coordination, which in turn is due to the existence of a lone-pair on the Sn ion[59] that inhibits a more symmetric five-fold coordination. Since lone pairs exist even at the monolayer limit, van der Waals corrections may be needed for monolayers too. The lone pair is quenched to some extent on heavier monochalcogenides with a rhombic unit cells such as SnTe, but it can still have significant effects on their structural anisotropy at the monolayer limit,[25] that is missed within the PBE approximation.[26] (In fact, developers of van der Waals functionals refer to group IV monochalcogenides as a material family where such corrections may be relevant; c.f. Refs. 60 and 61).

This way, the Curie temperature of 326 K for a SnSe monolayer reported in Ref.[26] disagrees with the classic theoretical result, $T_c = 1.14 \times 50.3$ K, Eqn. (4), by about 600%. Noting that the constrained Model 2 has only two degenerate states instead of four, Potts prediction will turn into the prediction for an Ising system (i.e., the relation among T_c and J on a square lattice with two-degenerate structural ground states): $k_B T_c = 2.27J$, which still remains 212 K below the value reported by Fei and coworkers. (In looking for a close correspondence, one should not turn inconsistent and use J from a calculation with van der Waals corrections on an estimate of T_c obtained with a PBE exchange-correlation potential.)

An explanation for the large value of T_c in Ref. 26 will next be provided to solve contradicting accounts for the transition temperature, thus contributing to an unified framework to understand 2D structural transitions in these materials.

V. INCREASING THE TRANSITION TEMPERATURE WITH TENSILE STRAIN

MD calculations uncovering phase transitions on group-IV monochalcogenide monolayers that are based on a NPT ensemble[20,23] agree with experimental observation concerning the collapse of $\langle \Delta\alpha \rangle$, down to the critical exponent.[25] It will now be qualitatively shown on a 8×8 supercell how uniaxial strain permits raising T_c up to the large values reported in Model 2, where lattice parameters are not allowed to evolve with temperature. Such strain may be engineered, or created at the interface between the monochalcogenide monolayer and a substrate during growth.[25]

To this end, and as illustrated in Fig. 5(a), SnSe monolayers were subjected to a one or two percent uniaxial tensile strain along the direction defined by either $\mathbf{a}_1$ or $\mathbf{a}_2$ at zero temperature and relaxed, still at zero temperature, afterwards. Lattice parameters prior and after the structural optimization are reported in Table III.

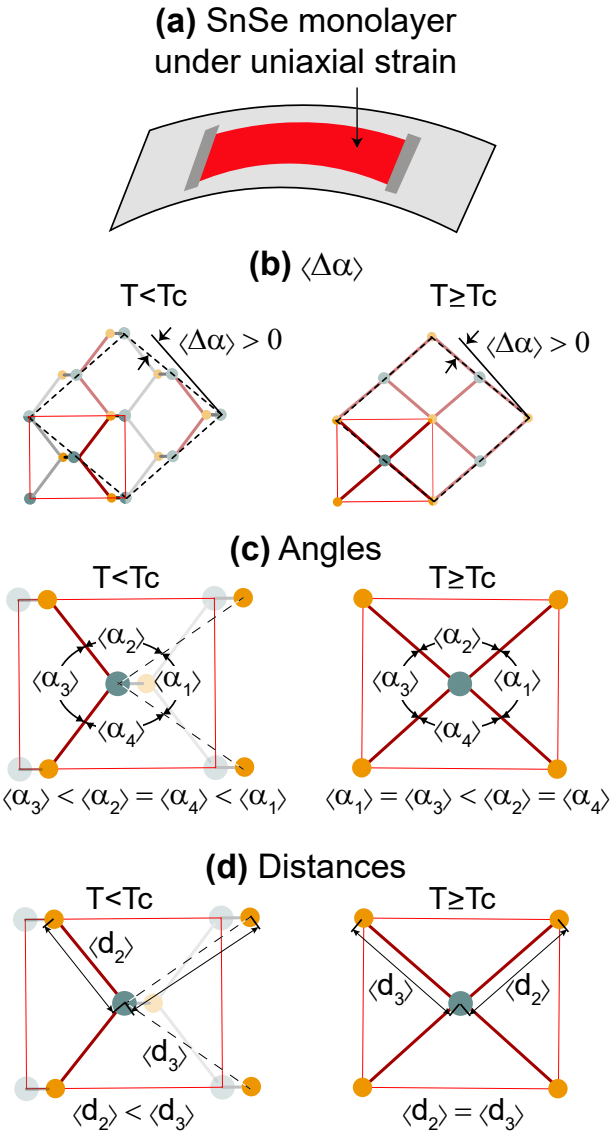

FIG. 5. (a) SnSe monolayer clamped onto a substrate and subjected to uniaxial tensile strain by bending. (b) to (c): proposed thermal evolution of $\langle \Delta\alpha \rangle$, $\langle \alpha_1 \rangle$, $\langle \alpha_2 \rangle$, $\langle \alpha_3 \rangle$, $\langle \alpha_4 \rangle$, $\langle d_2 \rangle$ and $\langle d_3 \rangle$. An explicit MD verification of this structural transition is given in Figs. 7 to 10.

Uniaxial strain impedes the creation of a square structure at T_c, and $\langle \Delta\alpha \rangle$ remains non-zero through the transition, as displayed in Fig. 5(b). The introduction of this symmetry-breaking constraint[62] reduces the original four-fold degeneracy onto a two-fold one.

As highlighted in Fig. 5(c) there are three dissimilar angles prior to the transition, and two dissimilar ones once the transition takes place. Similarly, as indicated in Fig. 5(d), $\langle d_2 \rangle$ and $\langle d_3 \rangle$ become equal at T_c. This happens as the tilt $\langle \delta \rangle$ and $\langle \theta \rangle$ both turn to zero, thus quenching the in-plane electric dipole too.

The structural transition described in Fig. 5 is the one argued for in Ref. 26, where only two degenerate ground

TABLE III. Lattice parameters of strained SnSe at zero temperature prior ($a_{1,0}$, $a_{2,0}$) and after (a_1, a_2) a structural optimization. Here, $\epsilon = \delta a_1/a_1$, or $\epsilon = \delta a_2/a_2$, accordingly.

ϵ	$a_{1,0}$ (Å)	$a_{2,0}$ (Å)	$\frac{a_{1,0}}{a_{2,0}}$	a_1 (Å)	a_2 (Å)	$\frac{a_1}{a_2}$
0.01 (a_1)	4.5160	4.3264	1.044	4.5160	4.3200	1.045
0.02 (a_1)	4.5600	4.3264	1.054	4.5600	4.3020	1.060
0.01 (a_2)	4.4873	4.3750	1.026	4.4400	4.3750	1.015
0.02 (a_2)	4.4873	4.4191	1.015	4.3551	4.4191	0.986

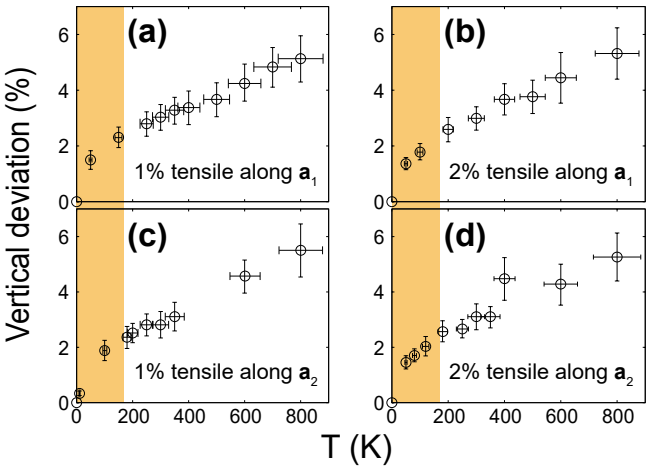

FIG. 6. Vertical displacements of samples under uniaxial strain. The value of T_c on the 8×8 unstrained sample (175 K) is emphasized by a yellow rectangle.

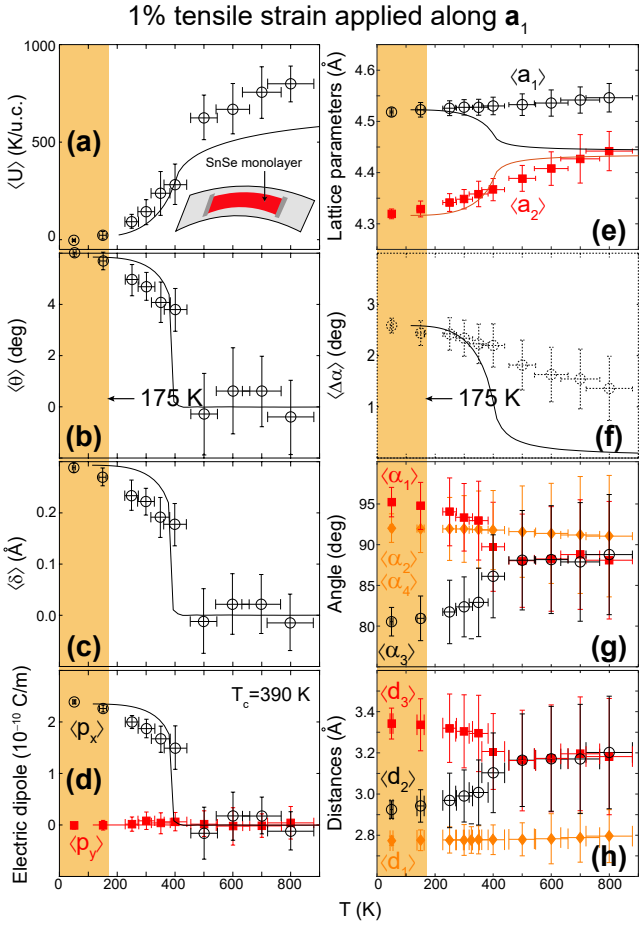

FIG. 7. Structural transition of a SnSe monolayer under an initial 1% uniaxial tensile strain along a_1: while T_c is signalled by the sudden agreement of lattice parameters ($\langle a_1 \rangle = \langle a_2 \rangle$) and the collapse of $\langle \Delta\alpha \rangle$ on unstrained samples, a strained sample preserves a rectangular shape. Nevertheless, its intrinsic dipole turns to zero as in-plane angles and distances take on two values for $T \geq T_c$, instead of three for $T < T_c$. The value of T_c on the 8×8 unstrained sample (175 K) is emphasized by the yellow rectangle. Fitting curves are thermodynamical averages arising from Eqn. 10.

states exist. It will be explicitly verified through MD calculations on uniaxially-strained samples in Figs. 7 to 10, that display the configurational energy $\langle U \rangle$, the electric dipole, and structural order parameters that include $\langle \theta \rangle$, $\langle \delta \rangle$, lattice parameters $\langle a_1 \rangle$ and $\langle a_2 \rangle$, as well as the parameters $\langle \Delta\alpha \rangle$, angles and distances that were highlighted in Figs. 5(b-d).

Similar to previous studies on non-strained samples, an 8×8 supercell is built out of the strained unit cells at zero temperature afterwards, and the MD simulation box is kept fixed along the strained direction throughout the thermal evolution, by an in-house modification of the computational tool. MD calculations on the NPT ensemble ran for over 30,000 femtoseconds at selected temperatures. One sees in Fig. 6 a relative increase of out-of-plane corrugations when contrasted with Fig. 3(a), which is due to the larger temperature range employed in runs dealing with samples under strain. In Fig. 6, no signature of the transition can be extracted from out-of-plane corrugations.

Figure 7 displays a 2D structural phase transition of a SnSe monolayer under 1% tensile uniaxial strain along a_1 that is captured in Fig. 7(a) by a sudden increase of $\langle U \rangle$ at a $T_c = 390$ K that is higher than its $T_c = 175$ K value in Fig. 3(a) and is a result of the structural constraint. The saturation value of $\langle U \rangle$ is also larger than that seen in Fig. 3(a).

The order parameters $\langle \theta \rangle$, $\langle \delta \rangle$ and the electric dipole $\langle p_x \rangle$ show an identical dependence on temperature in Figs. 7(b-d). These identical trends can be understood from the fact that $\langle \delta \rangle$ is the in-plane separation among the positive group-IV element and the negative chalcogen (e.g., atoms $\mathbf{b}_2$ and $\mathbf{b}_3$), that turns the in-plane electric dipole $\langle p_x \rangle$ on, while $\langle \theta \rangle$ is linearly proportional to $\langle \delta \rangle$ for small angles.

The lattice parameter $\langle a_1 \rangle$ in Fig. 7(e) can be obtained either from the fixed length of the constrained supercell, or from the distance among identical basis atoms belonging to consecutive unit cells. The second choice, displayed in Figs. 7 through 10, permits adding information about out-of-plane oscillations at finite temperature and confers $\langle a_1 \rangle$ with a slight slope and an error bar.

The orthogonal and unconstrained lattice vector $\mathbf{a}_2$ in-

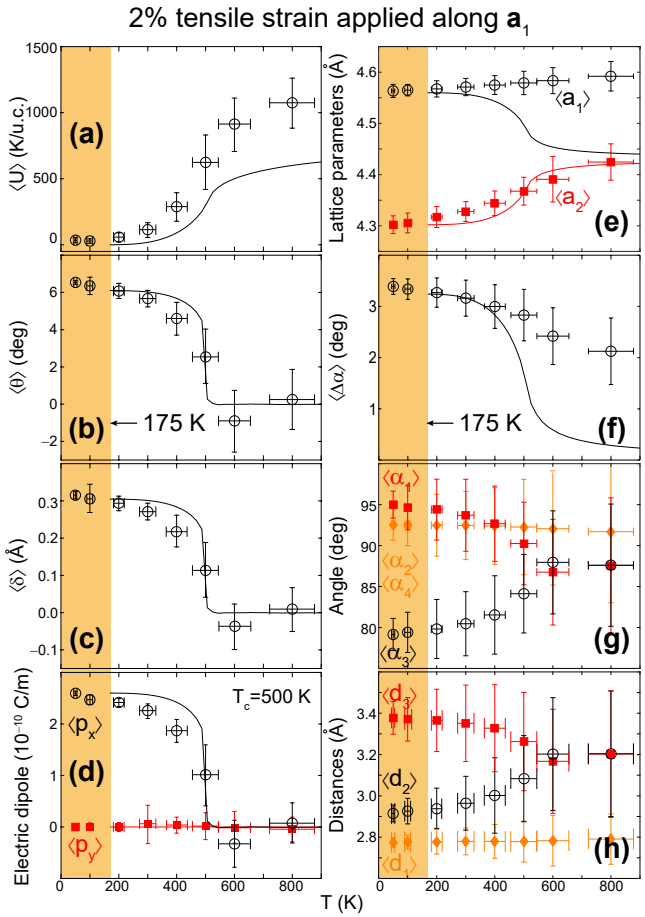

FIG. 8. Structural transition of a SnSe monolayer under an initial 2% uniaxial tensile strain along a_1, that raises T_c to 470 K. The value of T_c on the 8×8 unstrained sample (175 K) is emphasized by the yellow rectangle. Fitting curves are thermodynamical averages arising from Eqn. 10.

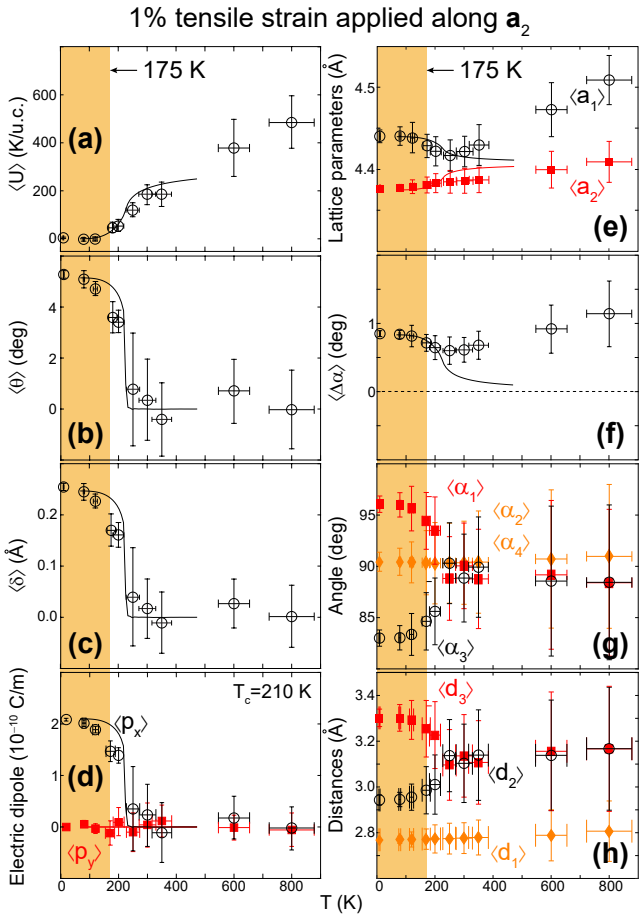

FIG. 9. SnSe monolayer under 1% uniaxial strain along a_2: given that the transition still occurs outside of the yellow-marked areas, T_c still increases when the shorter lattice parameter a_2 was elongated by 1%. The value of T_c on the 8×8 unstrained sample (175 K) is emphasized by the yellow rectangle. Fitting curves are thermodynamical averages arising from Eqn. 10.

creases its magnitude with temperature due to a positive coefficient of thermal expansion. Nevertheless, $\langle \Delta\alpha \rangle$ in Fig. 7(f) remains non-zero through this transition: $\langle \Delta\alpha \rangle$ is not a good measure for the structural transition of strained samples that are never let to turn onto square unit cells artificially in numerical calculations.

Despite of the lack of converging values of $\langle \Delta\alpha \rangle$ to 0 in Fig. 7(e), Figs. 7(g) and 7(h) show a convergence of $\langle \alpha_1 \rangle$ onto $\langle \alpha_3 \rangle$ at T_c that is similar to the one shown in Fig. 5(c). Similarly, $\langle d_2 \rangle = \langle d_3 \rangle$ at T_c in Fig. 7(h), which is consistent with the transition depicted in Fig. 5(d).

Given that $\langle p_x \rangle$ is quenched in Fig. 7(d), the transition of a group-IV monolayer under uniaxial tensile strain bears resemblance to a transition on a NVT ensemble;[26] the exception being the release of a_2 to vary, a condition consistent with a SnSe monolayer clamped at two opposite ends only.

Figure 8 shows the structural transition when the strain is raised to a still small value of 2%. The transition is similar to the one described in Fig. 7, but now $\langle U \rangle$ doubles it value when compared to its magnitude in Fig. 7 while T_c continues to increase, thus demonstrating the high degree of tunability of T_c with moderate tensile strain.

Compressive strain is hard to achieve in 2D materials, but as seen in Fig. 9, tensile strained can also be applied along the short lattice vector a_2, thus favoring a square structure. The larger magnitude of T_c in Fig. 9 indicates that any constraint on the original four-fold degenerate structure increases T_c. As discussed before,[20] an unstrained unit cell requires two "turning events" to switch its polarization by 180 degree: a direct flip of polarization from $A_{\rightarrow}$ to $A_{\leftarrow}$ requires an energy of $2J$, while a two-step flip (either $A_{\rightarrow}$ to $B_{\uparrow}$ to $A_{\leftarrow}$, or $A_{\rightarrow}$ to $B_{\downarrow}$ to $A_{\leftarrow}$) only requires overcoming a barrier equal to J at each 90-degree flip. In favoring a pair of degenerate ground states over the other two, one reduces the probability of the two-step transition to favor a transition

through the larger ($2J$) barrier, hence raising T_c.

Fig. 9 is similar to Figs. 7 and 8, but Fig. 9(e) shows a decrease of $\langle a_1 \rangle$ towards $\langle a_2 \rangle$ that is suddenly suppressed at higher temperature. The sudden change of $\langle a_1 \rangle$ and $\langle a_2 \rangle$ with temperature is due to the thermal softening of elastic constants in these 2D materials.

VI. SETTING THE ORIENTATION OF THE ELECTRIC DIPOLE WITH TENSILE STRAIN

$\langle a_1 \rangle$ is larger than $\langle a_2 \rangle$ in Figs. 7 through 9. Nevertheless, the SnSe monolayer aligns its in-plane dipole under a threshold uniaxial tensile strain along a_2, to become parallel to the direction of the external uniaxial tensile strain: uniaxial tensile strain can be used to orient the direction of the intrinsic in-plane electric field.

As shown in Table III and Fig. 10, a 2% strain along the initially smaller in-plane lattice vector a_2 is sufficient to make a_2 larger than a_1, and MD calculations indicate that the electric dipole realigns to be parallel to the $y-$direction: in Fig. 10, angles $\langle \alpha_2 \rangle$ and $\langle \alpha_4 \rangle$ take on dissimilar values at zero temperature, and converge at T_c, while $\langle \alpha_1 \rangle$ and $\langle \alpha_3 \rangle$ remain identical through the transition. In contrast, Figs. 7(e), 8(e) and 9(e) display different magnitudes of $\langle \alpha_1 \rangle$ and $\langle \alpha_3 \rangle$ at zero temperature that converge at T_c, while $\langle \alpha_2 \rangle$ and $\langle \alpha_4 \rangle$ remain identical, while the in-plane electric dipole was oriented along the $x-$direction. T_c is raised to 250 K in this scenario.

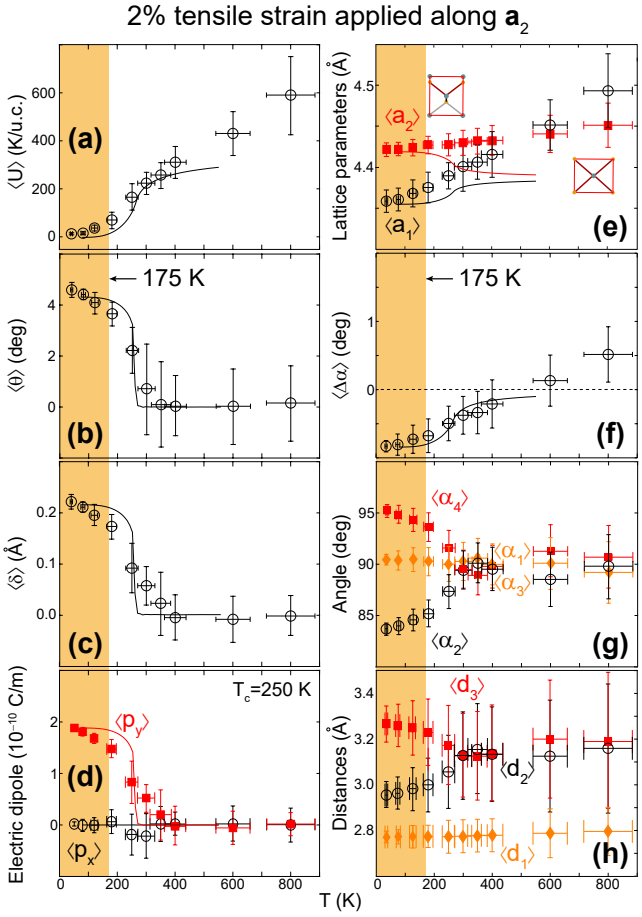

FIG. 10. 8×8 SnSe monolayer supercell under 2% uniaxial strain along a_2: as the transition occurs for T_c outside the yellow box, T_c still increases when the shorter lattice parameter is elongated by 2%, the orientation of the electric dipole flips in order to point along the longest lattice vector, making $\langle \delta \rangle$ align along the $y-$direction in subplot (c), so that $\langle p_y \rangle$ is non-zero in subplot (d). (e) $\langle a_1 \rangle$ becomes larger than $\langle a_2 \rangle$ again at a temperature larger than T_c, making $\langle \Delta\alpha \rangle$ in subplot (f) change sign. The dipole orientation along the $y-$axis comes about from the angles in subplot (g) that are different before T_c, when compared with those in Figs. 7 to 9. Fitting curves are thermodynamical averages arising from Eqn. 10 (T_c on the 8×8 unstrained sample (175 K) is emphasized by the yellow rectangle).

VII. PHASE TRANSITION OF STRAINED MONOLAYERS IN A TWO-PARAMETER MODEL

A clock model with one single fitting parameter J allows to understand the phenomenology of unstrained group-IV monochalcogenides qualitatively. In order to emphasize the basic physical behavior over numerical details, we wish to maintain the simplicity of that model in describing strained monolayers.

As indicated in Section IV, the relation among T_c and J increases by decreasing the number of degenerate ground states. This observation implies that the increase of T_c observed in Figs. 7 to 10 with respect to its magnitude on an unstrained sample, could in principle be assigned to the favoring of two structural ground states (*i.e.*, those two parallel to the applied strain ϵ) and makes it more energy costly to occupy the two states whose dipole moments $\mathbf{p}_i$ are parallel to the direction of the applied strain. An interaction of the form $-|\mathbf{p}_i(\epsilon) \cdot \epsilon|$ enforces the preference of two degenerate states over the other two, and sets the system in between a Potts model with four degenerate ground states when previous term is turned off, and an Ising model when this term is on and set larger than J, such that $T_c \sim [1.1(4) - 2.2(7)]J$ depending on the magnitude of strain. Previous statements imply that strain lowers the initial symmetry of the structure and lowers the number of degenerate ground states.[62]. The preference of two states over the other two implies that a square structure is not found at T_c as well, such that $|langle\Delta\alpha\rangle| > 0$ at T_c.

This way, the effective dynamics of strained samples takes the following form:

$$U = -J \sum_i \left(1 - \sum_{\langle i,j \rangle} \cos(\Theta_i - \Theta_j) \right) - h \sum_i |\mathbf{p}_i(\epsilon) \cdot \epsilon|, \tag{10}$$

where i runs over $n-$individual sites, $\langle i, j \rangle$ implies a

sum over next-nearest neighbors, and Θ_i is the (discrete) dipole orientation, which can take on four values that correspond to the four degenerate ground states on the unstrained sample, and h is an additional fitting parameter.

The first term to the right of Eqn. (10) is similar to the one given in Ref.[20]. As discussed earlier, the second term reduces the original four-fold degeneracy because it favors orientations of the electric dipole that are parallel to the direction of the applied strain, turning the system into an Ising (two-fold degenerate) lattice, and hence yielding T_c in between $1.14J$ when the first term dominates and $2.27J$ when the second term does. We consider strain ϵ parallel to either $\mathbf{a}_1$ or $\mathbf{a}_2$ and dipole moments pointing parallel or anti-parallel to the lattice vectors.

The dynamics expressed by Eqn. (10) were employed in an in-house Monte Carlo solver on a 60×60 supercell, and the solid trendlines in Figs. 7 through 10 are results from the model that fully describe the MD phenomenology. In order for the model to best describe MD data, we found it necessary to increase the magnitude of J. This is, strain sets a preference for two degenerate ground states, but it also increases the elastic energy barrier. The parameters employed in obtaining the dashed curves in Figs. 7 through 10 are listed in Table IV.

$\langle U\rangle$ is the expectation value of U given in Eqn. (10), and writing the probability of a given dipole orientation as $\langle\rightarrow\rangle$, $\langle\leftarrow\rangle$, $\langle\uparrow\rangle$ and $\langle\downarrow\rangle$, which are all functions of temperature, condition 2 in Section 1 is established by setting $\langle\rightarrow\rangle = 1$ at zero temperature. This way, the lattice parameters and other order parameters are estimated by:

$$\langle a_1(\boldsymbol{\epsilon})\rangle = \frac{a_1(T=0,\boldsymbol{\epsilon})(\langle\rightarrow\rangle+\langle\leftarrow\rangle)+a_2(T=0,\boldsymbol{\epsilon})(\langle\uparrow\rangle+\langle\downarrow\rangle)}{\langle\rightarrow\rangle+\langle\leftarrow\rangle+\langle\uparrow\rangle+\langle\downarrow\rangle},$$

$$\langle a_2(\boldsymbol{\epsilon})\rangle = \frac{a_1(T=0,\boldsymbol{\epsilon})(\langle\uparrow\rangle+\langle\downarrow\rangle)+a_2(T=0,\boldsymbol{\epsilon})(\langle\rightarrow\rangle+\langle\leftarrow\rangle)}{\langle\rightarrow\rangle+\langle\leftarrow\rangle+\langle\uparrow\rangle+\langle\downarrow\rangle},$$

$$\langle\Delta\alpha(\boldsymbol{\epsilon})\rangle = \frac{\langle a_1(\boldsymbol{\epsilon})\rangle}{\langle a_2(\boldsymbol{\epsilon})\rangle} - 1,$$

$$\langle p_x(\boldsymbol{\epsilon})\rangle = \frac{p_x(T=0,\boldsymbol{\epsilon})(\langle\rightarrow\rangle-\langle\leftarrow\rangle)}{\langle\rightarrow\rangle+\langle\leftarrow\rangle+\langle\uparrow\rangle+\langle\downarrow\rangle},$$

and

$$\langle p_y(\boldsymbol{\epsilon})\rangle = \frac{p_x(T=0,\boldsymbol{\epsilon})(\langle\uparrow\rangle-\langle\downarrow\rangle)}{\langle\rightarrow\rangle+\langle\leftarrow\rangle+\langle\uparrow\rangle+\langle\downarrow\rangle},$$

and shown by solid curves in Figs. 3 (for $\boldsymbol{\epsilon}=\mathbf{0}$, $J=150$ K, and $h=0$), and 7 to 10. There, $\langle\theta\rangle$ and $\langle\delta\rangle$ are proportional to $\langle\mathbf{p}\rangle$, and the zero-temperature values are taken from Table III. The qualitative agreement among the full-scale MD data and the results from the model stands out given the simplicity of the latter: though the model could be improved, it captures the essential effects of strain on structure.

TABLE IV. Magnitudes of model parameters and T_c.

ϵ	J (K)	h ($10^{10}\frac{Km}{C}$)	p_x ($10^{-10}\frac{C}{m}$)	δ (Å)	θ (deg)	T_c (K)
0.01 (a_1)	330	25.53	2.35	0.295	5.9	390
0.02 (a_1)	375	38.46	2.60	0.305	6.1	500
0.01 (a_2)	175	5.00	2.00	0.270	5.4	210
0.02 (a_2)	175	51.28	1.95	0.215	4.3	250

VIII. CONCLUSIONS

To conclude, this manuscript improves the present understanding of two-dimensional structural phase transitions on two-dimensional materials beyond graphene.

The conditions for 2D structural transitions are: the existence of degeneracies on the ground state unit cell, a path among degenerate ground states that has an energy barrier smaller than the melting point, and the existence of sufficiently large monodomains displaying a given ground state.

Unstrained group-IV monochalcogenide monolayers possess four switchable ground states. These materials undergo a 2D structural transition at finite temperature provided the lattice parameters evolve freely and unconstrained, such that all four ground states are sampled. Sampling of the four ground states is essential for theory to describe experimentally-observed transitions that are triggered by the collapse of $\langle\Delta\alpha\rangle$ to zero and possess a critical exponent $\beta = 1/3$.

Constraining the unit cell lattice vectors to their magnitude at zero temperature while discussing finite-temperature properties amounts to applying strain and it raises the transition temperature from its magnitude on an *intrinsic*, unstrained sample.

The transition temperature, and even the orientation of the in-plane intrinsic electric dipole can be widely controlled by moderate uniaxial tensile strain. These MD results can be qualitatively cast onto an extension of the clock model. Additional studies may include the amount of entropy in these systems at finite temperature.

The results from the present study will assist in establishing a solid theoretical background for further work in phase transitions in two-dimensional materials, and their effects on material properties, and offer intriguing connections among topics in soft-condensed matter and novel two-dimensional atomic materials.

This work was funded by an Early Career Grant from the DOE (DE-SC0016139; S.B.L. and T.P.K). Calculations were performed at Arkansas High Performance Computing Center's *Trestles*, which is funded through multiple National Science Foundation grants and the Arkansas Economic Development Commission. Conversations with Kai Chang are gratefully acknowledged.

Appendix A: Further details of methods employed

The energy landscape and the dependency of order parameters of SnSe monolayers on r in Figs. 1 and 2 were obtained with the *SIESTA* DFT code[27] in calculations carried out on the unit cell at zero temperature and with van der Waals corrections within the consistent-exchange vdW-DF-cx functional[55]. The pseudopotentials with van der Waals corrections have cutoff radii as listed for PBE pseudos in Ref.[17]. Calculations proceeded with a 18×18 $k-$point grid, and a mesh cutoff of 300 Ry for the Poisson solver was employed as well. The mesh from which Fig. 1(a) was drawn included 50 independent values of a_1 and a_2. As indicated in the main text, the unit cells along the $a_1 = a_2$ line were obtained on structures that have an explicit zero net in-plane dipole.

The structures listed in Tables I and II were obtained with the *SIESTA*, *VASP*[45], and *Quantum Espresso*[49] computer codes, as listed.

All results obtained within plane-wave, pseudopotential density-functional theory methods (e.g., *VASP* and *Quantum Espresso*) employ projector-augmented wave[63] pseudopotentials that are tuned against the open-source pseudopotential library.[64,65].

The calculations within *VASP* employ a 15 × 15 $k-$point grid and a cutoff energy of 37 Ry. The force convergence criteria was set to 10^{-3} eV/Å. In *Quantum Espresso* calculations a 15 × 15 $k-$point grid was also employed, with cutoff energy of 40 Ry, and a force convergence criteria of 10^{-4} eV/Å. van der Waals corrections in the *VASP* code were turned on by employing the following flags: $GGA = OR$; $LUSE\_VDW = .TRUE.$, and $AGGAC = 0.0000$. Espresso calculations with van der Waals corrections employed the $vdW - DF - obk8$ flag.

The landscape shown in Fig. 1(a) is extremely flat near the local minima for a regular force minimization process with standard limits (e.g., a force tolerance of 0.001 eV/AA) to reach the lowest-energy configuration. For this reason, a meshing of a_1 and a_2 around the minimum-energy structures was employed to truly guarantee that the absolute minima had been reached. This should help reduce the current spread in known structural estimates.

Figure 3(e) re-expresses results from previous calculations[23] in the language of Refs. 25 and 26. These results were obtained from *ab initio* MD calculations with the *SIESTA* code that were performed on the NPT ensemble, with basis sets and input parameters similar to those listed in previous paragraph for consistency.

NPT MD calculations at standard ambient pressure proceed with an algorithm in which temperature is controlled by a Nose thermostat, while pressure is controlled using the Parinello-Raman method.[66] The original method is contained in the `dynamics.F` file of the *SIESTA* distribution.

The standard algorithm on file pushes all six containing walls, including those not in direct contact with the 2D material. Therefore, a physically meaningful constraint is imposed, such that the lattice vector perpendicular to the supercell, $\mathbf{a}_3$, is not a function of time. Calculations on samples under uniaxial strain proceed by setting the time evolution of an additional, in-plane superlattice vector (i.e., $8\mathbf{a_1}$) to zero as well, while the remaining superlattice vector (i.e., $8\mathbf{a_2}$) is let to vary with time. The algorithm can be shared with any interested party, and additional details will be provided in a separate publication.

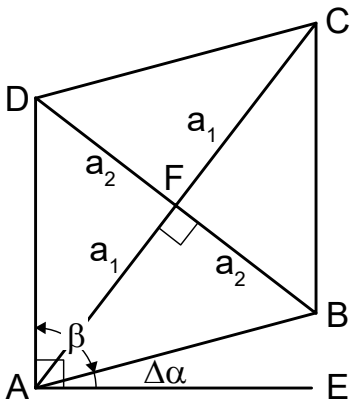

FIG. 11. Geometrical parameters on a rhombus that were employed to derive Eqn. (1) of the main text.

Table II lists structural parameters for a SnSe monolayer with the *VASP* code within the PBE[57] approximation for exchange-correlation. Here, we restate the existence of a systematic underestimation of the ratio a_1/a_2 in DFT calculations that can be expressed as follows:

$$1 \leq (a_1/a_2)_{LDA} < (a_1/a_2)_{PBE} < (a_1/a_2)_{vdW}.$$

The results in Figs. 7 through 10 where obtained with the *SIESTA* code using input parameters that are similar to those listed two paragraphs above.

Numerical limitations in the theoretical understanding of group-IV monochalcogenides must also be properly acknowledged in order to foresee opportunities for further work. For example, the magnitude of J could be contrasted against other van der Waals implementations,[67,68] other approaches like Quantum Montecarlo,[69] and available experiments.[25] Similar to status of bulk ferroelectrics, experimental and theory-based transition temperatures tend not to be in perfect agreement, which does not preclude a complete theoretical description of the fundamental physical picture at hand.

Appendix B: Relation among a_1/a_2 and $\Delta\alpha$

The rhombus in Fig. 2(a) –that is reproduced in Fig. 11– has sides AB, BC, CD, and DA of equal length a, but angles $\angle DAB = \angle BCD < 90^o < \angle ABC = \angle CDA$. It also has two orthogonal diagonals $BD < AC$.

Given that $\angle EAD = 90^o$, $\Delta\alpha$ measures the deviation from a square structure. ($\Delta\alpha = 0^o$ implies $\angle DAB = \angle BCD = \angle ABC = \angle CDA = 90^o$, and $BD = AC$; *i.e.*, a square.)

$\beta + \Delta\alpha = 90^o$ in Fig. 11 yields $\beta/2 = 45^o - \Delta\alpha/2$. Orthogonality of diagonals further implies that $\frac{a_1}{a_2} = \cot\left(\frac{\beta}{2}\right) = \cot\left(45^o - \frac{\Delta\alpha}{2}\right)$. Now, $\cos(45^o) = \sin(45^o) = 1/\sqrt{2}$, so that:

$$\frac{a_1}{a_2} = \frac{\cos\left(\frac{\Delta\alpha}{2}\right) + \sin\left(\frac{\Delta\alpha}{2}\right)}{\cos\left(\frac{\Delta\alpha}{2}\right) - \sin\left(\frac{\Delta\alpha}{2}\right)}.$$

Multiplying both the numerator and denominator by $\cos\left(\frac{\Delta\alpha}{2}\right) + \sin\left(\frac{\Delta\alpha}{2}\right)$ yields:

$$\frac{a_1}{a_2} = \frac{1 + 2\cos\left(\frac{\Delta\alpha}{2}\right)\sin\left(\frac{\Delta\alpha}{2}\right)}{\cos^2\left(\frac{\Delta\alpha}{2}\right) - \sin^2\left(\frac{\Delta\alpha}{2}\right)} = \frac{1 + \sin(\Delta\alpha)}{\cos(\Delta\alpha)},$$

which is Eqn. (1) of the main text.

* sbarraza@uark.edu

[1] A. Fasolino, J. H. Los, and M. I. Katsnelson, Nat. Mater. **6**, 858 (2007).
[2] J. Meyer, A. Geim, M. Katsnelson, K. Novoselov, T. Booth, and S. Roth, Nature **446**, 60 (2007).
[3] J. Brivio, D. T. L. Alexander, and A. Kis, Nano Lett. **11**, 5148 (2011).
[4] P. Miró, M. Ghorbani-Asl, and T. Heine, Adv. Mat. **25**, 5473 (2013).
[5] R. B. Potts, Math. Proc. Camb. Phil. Soc. **48**, 106 (1952).
[6] R. Houtappel, Physica **16**, 425 (1950).
[7] N. D. Mermin and H. Wagner, Phys. Rev. Lett. **17**, 1133 (1966).
[8] D. Nelson, S. Weinberg, and T. Piran, *Statistical Mechanics of Membranes and Surfaces*, 2nd ed. (World Scientific, Singapore, 2004).
[9] E. Sutter, Y. Huang, H.-P. Komsa, M. Ghorbani-Asl, A. Krasheninnikov, and P. Sutter, Nano Lett. **16**, 4410 (2016).
[10] A. H. Castro Neto, F. Guinea, N. M. R. Peres, K. S. Novoselov, and A. K. Geim, Rev. Mod. Phys. **81**, 109 (2009).
[11] M. Katsnelson, *Graphene: Carbon in two dimensions*, 1st ed. (Cambridge University Press, 2012).
[12] P. Avouris, T. F. Heinz, and T. Low, *2D materials: properties and devices* (Cambridge U. Press, UK, 2017).
[13] A. Nagashima, N. Tejima, Y. Gamou, T. Kawai, and C. Oshima, Phys. Rev. Lett. **75**, 3918 (1995).
[14] S. Cahangirov, M. Topsakal, E. Aktürk, H. Şahin, and S. Ciraci, Phys. Rev. Lett. **102**, 236804 (2009).
[15] A. Kara, H. Enriquez, A. P. Seitsonen, L. L. Y. Voon, S. Vizzini, B. Aufray, and H. Oughaddou, Surf. Sci. Rep. **67**, 1 (2012).
[16] S. Chowdhury and D. Jana, Rep. Prog. Phys. **79**, 126501 (2016).
[17] P. Rivero, J.-A. Yan, V. M. García-Suárez, J. Ferrer, and S. Barraza-Lopez, Phys. Rev. B **90**, 241408 (2014).
[18] G. G. Naumis, S. Barraza-Lopez, M. Oliva-Leyva, and H. Terrones, Rep. Prog. Phys. **80**, 096501 (2017).
[19] W. Li and J. Li, Nat. Commun. **7**, 10843 (2016).
[20] M. Mehboudi, A. M. Dorio, W. Zhu, A. van der Zande, H. O. H. Churchill, A. A. Pacheco-Sanjuan, E. O. Harriss, P. Kumar, and S. Barraza-Lopez, Nano Lett. **16**, 1704 (2016).
[21] M. Wu and X. C. Zeng, Nano Lett. **16**, 3236 (2016).
[22] H. Wang and X. Qian, 2D Mat. **4**, 015042 (2017).
[23] M. Mehboudi, B. M. Fregoso, Y. Yang, W. Zhu, A. van der Zande, J. Ferrer, L. Bellaiche, P. Kumar, and S. Barraza-Lopez, Phys. Rev. Lett. **117**, 246802 (2016).
[24] C. Li, J. Hong, A. May, D. Bansal, S. Chi, T. Hong, G. Ehlers, and O. Delaire, Nat. Phys. **11**, 1063 (2015).
[25] K. Chang, J. Liu, H. Lin, N. Wang, K. Zhao, A. Zhang, F. Jin, Y. Zhong, X. Hu, W. Duan, Q. Zhang, L. Fu, Q.-K. Xue, X. Chen, and S.-H. Ji, Science **353**, 274 (2016).
[26] R. Fei, W. Kang, and L. Yang, Phys. Rev. Lett. **117**, 097601 (2016).
[27] J. M. Soler, E. Artacho, J. D. Gale, A. García, J. Junquera, P. Ordejón, and D. Sánchez-Portal, J. Phys.: Condens. Matter **14**, 2745 (2002).
[28] G. Román-Pérez and J. M. Soler, Phys. Rev. Lett. **103**, 096102 (2009).
[29] D. Wales, *Energy Landscapes: Applications to Clusters, Biomolecules and Glasses* (Cambridge U. Press, UK, 2001).
[30] A. A. Pacheco Sanjuan, M. Mehboudi, E. O. Harriss, H. Terrones, and S. Barraza-Lopez, ACS Nano **8**, 1136 (2014).
[31] A. A. Pacheco Sanjuan, Z. Wang, H. Pour Imani, M. Vanević, and S. Barraza-Lopez, Phys. Rev. B **89**, 121403(R) (2014).
[32] M. Mehboudi, K. Utt, H. Terrones, E. O. Harriss, A. A. Pacheco SanJuan, and S. Barraza-Lopez, Proc. Natl. Acad. Sci. (USA) **112**, 5888 (2015).
[33] A. I. Bobenko, P. Schröder, J. M. Sullivan, and G. M. Ziegler, eds., *Discrete Differential Geometry*, 1st ed., Oberwolfach Seminars, Vol. 38 (Birkhäuser, Basel, Switzerland, 2008).
[34] X. Mao, A. Souslov, C. I. Mendoza, and T. Lubensky, Nat. Commun. **6**, 5968 (2015).
[35] P. Zalden, M. J. Shu, F. Chen, X. Wu, Y. Zhu, H. Wen, S. Johnston, Z.-X. Shen, P. Landreman, M. Brongersma, S. W. Fong, H.-S. P. Wong, M.-J. Sher, P. Jost, M. Kaes, M. Salinga, A. von Hoegen, M. Wuttig, and A. M. Lindenberg, Phys. Rev. Lett. **117**, 067601 (2016).
[36] G. E. Volovik, *The Universe in a Helium Droplet* (Oxford U. Press, UK, 2009).
[37] T. Rangel, B. M. Fregoso, B. S. Mendoza, T. Morimoto, J. E. Moore, and J. B. Neaton, Phys. Rev. Lett. **119**, 067402 (2017).
[38] L. C. Gomes and A. Carvalho, Phys. Rev. B **92**, 085406 (2015).
[39] R. Fei, W. Li, J. Li, and L. Yang, Appl. Phys. Lett. **107**, 173104 (2015).
[40] L. Huang, F. Wu, and J. Li, J. Chem. Phys. **144**, 114708

(2016).
[41] A. K. Singh and R. G. Hennig, Appl. Phys. Lett. **105**, 042103 (2014).
[42] A. Shafique and Y.-H. Shin, Sci. Rep. **7**, 506 (2017).
[43] R. Haleoot, C. Paillard, T. P. Kaloni, M. Mehboudi, B. Xu, L. Bellaiche, and S. Barraza-Lopez, Phys. Rev. Lett. **118**, 227401 (2017).
[44] S.-D. Guo and Y.-H. Wang, J. Appl. Phys. **121**, 034302 (2017).
[45] G. Kresse and J. Furthmüller, Phys. Rev. B **54**, 11169 (1996).
[46] G. Kresse and D. Joubert, Phys. Rev. B **59**, 1758 (1999).
[47] J. Klimeš, D. R. Bowler, and A. Michaelides, J. Phys.: Condens. Matter **22**, 022201 (2010).
[48] J. Klimeš, D. R. Bowler, and A. Michaelides, Phys. Rev. B **83**, 195131 (2011).
[49] P. Giannozzi et al., J. Phys.: Condens. Matter **21**, 395502 (2009).
[50] P. E. Blöchl, Phys. Rev. B **50**, 17953 (1994).
[51] T. Thonhauser, V. R. Cooper, S. Li, A. Puzder, P. Hyldgaard, and D. C. Langreth, Phys. Rev. B **76**, 125112 (2007).
[52] T. Thonhauser, S. Zuluaga, C. A. Arter, K. Berland, E. Schröder, and P. Hyldgaard, Phys. Rev. Lett. **115**, 136402 (2015).
[53] D. Langreth, B. Lundqvist, S. Chakarova-Käck, V. Cooper, M. Dion, P. Hyldgaard, A. Kelkkanen, J. Kleis, L. Kong, S. Li, P. Moses, E. Murray, A. Puzder, H. Rydberg, E. Schröder, and T. Thonhauser, J. Phys.: Condens. Matter **21**, 084203 (2009).
[54] K. Berland, V. Cooper, K. Lee, E. Schröder, T. Thonhauser, P. Hyldgaard, and B. Lundqvist, Rep. Prog. Phys. **78**, 066501 (2015).
[55] K. Berland and P. Hyldgaard, Phys. Rev. B **89**, 035412 (2014).
[56] P. Rivero, V. M. García-Suárez, D. Pereniguez, K. Utt, Y. Yang, L. Bellaiche, K. Park, J. Ferrer, and S. Barraza-Lopez, Comp. Mat. Sci. **98**, 372 (2015).
[57] J. Perdew, K. Burke, and M. Ernzerhof, Phys. Rev. Lett. **77**, 3865 (1996).
[58] A. Antuek, M. Urban, and A. J. Sadlej, J. Chem. Phys. **119**, 7247 (2003).
[59] I. Lefebvre, M. A. Szymanski, J. Olivier-Fourcade, and J. C. Jumas, Phys. Rev. B **58**, 1896 (1998).
[60] E. Schroder, V. R. Cooper, K. Berland, B. I. Lundqvist, P. Hyldgaard, and T. Thonhauser, in *Non-Covalent Interactions in Quantum Chemistry and Physics*, edited by A. O. d. l. Roza, , and G. A. DiLabio (Elsevier, 2017) pp. 241 – 274.
[61] L. Gharaee, P. Erhart, and P. Hyldgaard, Phys. Rev. B **95**, 085147 (2017).
[62] J. V. José, L. P. Kadanoff, S. Kirkpatrick, and D. R. Nelson, Phys. Rev. B **16**, 1217 (1977).
[63] P. E. Blöchl, Phys. Rev. B **50**, 17953 (1994).
[64] G. Kresse and D. Joubert, Phys. Rev. B **59**, 1758 (1999).
[65] K. Garrity, J. Bennett, K. Rabe, and D. Vanderbilt, Comput. Mater. Sci. , 446 (2014) **81**, 446 (2014).
[66] M. A. and D. J. Tildesley, *Computer Simulation of Liquids*, 2nd ed. (Oxford U. Press, 2017).
[67] E. Schröder, V. Cooper, K. Berland, B. Lundqvist, P. Hyldgaard, and T. Thonhauser, "Non-covalent interactions in quantum chemistry and physics: Theory and applications," (Elsevier, Amsterdam, 2017) Chap. The vdW-DF Family of Nonlocal Exchange-Correlation Functionals, pp. 241–274.
[68] L. Gharaee, P. Erhart, and P. Hyldgaard, Phys. Rev. B **95**, 085147 (2017).
[69] L. Shulenburger, A. Baczewski, Z. Zhu, J. Guan, and D. Tománek, Nano Lett. **15**, 8170 (2015).